1   **Assessing water vapor tomography in Hong Kong with improved vertical and**

2   **horizontal constraints**

3   **Pengfei Xia[1,2⊠], Shirong Ye[1], Peng Jiang[3], Lin Pan[2,4], Min Guo[5]**

4   [1]GNSS Research Center, Wuhan University, Wuhan 430079, China

5   [2]Key Laboratory of Geospace Environment and Geodesy, Ministry of Education,

6   Wuhan University, 129 Luoyu Road, Wuhan 430079, China

7   [3]School of Resources and Environmental Engineering, Anhui University, Hefei,

8   230601

9   [4]School of Geodesy and Geomatics, Wuhan University, 129 Luoyu Road, Wuhan

10   430079, China

11   [5]School of Surveying and Land Information Engineering, Henan Polytechnic

12   University, Jiaozuo 454000, China

13   *Correspondence to:* Pengfei Xia (xpf130@163.com); Ye Shirong (*srye@whu.edu.cn*)

14   **Abstract:** In this study, we focused on the retrieval of atmospheric water vapor

15   density by optimizing the tomography technique. First, we established a new

16   atmospheric weighted average temperature model that considers the effects of

17   temperature and height, assisted by Constellation Observing System for Meteorology,

18   Ionosphere and Climate (COSMIC) products. Next, we proposed a new method to

19   determine the scale height of water vapor, which will improve the quality of vertical

20   constraints. Finally, we determined the smoothing factor in the horizontal constraint

21   based on Interim European Centre for Medium-Range Weather Forecasts (ECMWF)

22   Re-Analysis (ERA-Interim) products. To evaluate the advantages of the optimized

23   technique over the traditional method, we used GPS datasets collected in Hong Kong

24   in August 2016 to estimate the vertical distribution of water vapor density using both

25   methods. We further validated the tomography results from the optimized technique

26 using radiosonde products. The results show that the water vapor density quality

27 obtained by the optimized technique is 13.8% better below 3.8 km and 8.1% better

28 above 3.8 km than that obtained by the traditional technique. We computed the

29 success rate of the tomography technique based on the Pearson product-moment

30 correlation coefficient (PCC) and root mean square (RMS). The success rate of the

31 optimized topography technique was approximately 10% higher than that of the

32 traditional tomography method.

33 **Keywords:** GPS radio occultation; water vapor; GPS tomography; atmospheric

34 weighted average temperature

35 **Introduction**

36 GPS technology has recently started being used to detect the Earth's atmosphere.

37 Many studies have been carried out to retrieve the two-dimensional (2D) or

38 three-dimensional (3D) distribution of atmospheric water vapor (Flores et al., 2001;

39 Champollion et al., 2005; Nilsson et al., 2006; Jin et al., 2009; Esteban et al., 2013;

40 Jiang et al., 2014; Chen et al., 2014). The obtained atmospheric water vapor product

41 can be assimilated into a numerical weather prediction (NWP) model. By applying the

42 NWP model to weather forecasting, we have discovered the usefulness of GPS

43 tomography to estimate water vapor distribution (Jin et al., 2011; Esteban et al., 2013).

44 Combined with the space-based GNSS (Global Navigation Satellite System)

45 occultation technique, it can provide neutral atmosphere products with high precision,

46 high vertical resolution, and low-cost, near-real-time, all-weather global coverage. In

47 addition, it can contribute to scientific research on the ionosphere (Kursinski et al.,

48 1997; Rocken et al., 1997; Hajj et al., 2002; Kuo et al., 2007).

49   In ground-based GPS meteorology, GPS signal propagation through the atmosphere

50   is slowed, thus causing path delay on the GPS measurements, which is termed

51   tropospheric delay (Kouba and Héroux, 2001). Zenith total delay (ZTD) is one of the

52   most important error sources in GNSS navigation and positioning; however, it is a

53   very reliable information source in GNSS meteorology (Jacob et al., 2007; Jin et al;

54   2007; Jin et al; 2009; Falconer et al., 2009). ZTD consists of two parts: zenith wet

55   delay (ZWD) and zenith hydrostatic delay (ZHD) (Davis et al., 1985). Usually, ZHD

56   can be calculated with high accuracy from empirical models, and ZWD can then be

57   easily derived from ZTD based on formula ZWD=ZTD-ZHD. Afterward, slant wet

58   delay (SWD) can be obtained from ZWD based on the wet Niell mapping function

59   (Niell, 1996). Both ZWD and SWD are related to atmosphere water vapor, and thus

60   precipitable water vapor (PWV) and slant water vapor (SWV) can be derived from

61   ZWD and SWD using the humidity conversion coefficient (Song, 2004).

62   ZHD is usually estimated in GNSS meteorological research using the Saastamoinen

63   model (Flores et al., 2000; Troller et al., 2006; Champollion et al., 2009; Perler et al.,

64   2011; Jiang et al., 2014). The atmospheric weighted mean temperature T_m is the key

65   variable to obtain high-precision humidity conversion coefficient (Mateus et al., 2014).

66   T_m will differ significantly as the season varies and the region changes (Jin et al.,

67   2008). It can be determined by the surface temperature measurement, which is

68   provided by a radiosonde product or other meteorological data analyses (Bevis et al.,

69   1992; Wang et al., 2011).

70   In space-based GNSS meteorology, GNSS radio occultation (RO) is regarded as a

71 valuable data source for atmospheric change studies (Rocken et al., 1997; Kursinski et

72 al., 1997; Hajj et al., 2002; Beyerle et al., 2005). The Constellation Observing System

73 for Meteorology, Ionosphere and Climate (COSMIC) is housed within the University

74 COporation for Atmospheric Research (UCAR). The mission of the COSMIC RO is

75 to develop the weather, climate, space weather and geodetic research (Yen et al.,

76 2007). The University Corporation for Atmospheric Research/COSMIC Data

77 Analysis and Archive Center (UCAR/CDAAC) supplies two different types of

78 products from the COSMIC mission: real-time data and post-processed data products.

79 Of these post-processed products, wet atmospheric profiles (wetPrfs) offer water

80 vapor pressure, temperature, etc. Shi et al. (2009) compared the bias of PWV between

81 wetPrf-derived and precise point positioning (PPP)–derived data and suggested that

82 they have comparable accuracy levels. Kishore et al. (2011) discussed the difference

83 in specific humidity between wetPrfs and radiosonde data. They concluded that both

84 sources have good correlation (~0.8) up to 8 km and that the humidity information of

85 wetPrfs is reliable up to nearly 8 km. In addition, Wang et al. (2013) studied the

86 accuracy of wetPrfs using the Radiosonde products as the reference and revealed that

87 a global mean temperature deviation of -0.09 K and a global mean humidity deviation

88 is better than -0.12 g/kg in the pressure range of 925 to 200 hPa.

89 To improve the accuracy of water vapor derived using the GNSS technique, we

90 optimized several key techniques for GNSS tomography. First, we precisely derived

91 the T_m model using wetPrf profiles, then determined the regional humidity conversion

92 coefficient. Next, for vertical constraints, we used a new way to determine the scale

93   height of water vapor in the exponential model. Finally, we derived the smoothing

94   factors of the Gauss distance weighting function in the horizontal constraint using

95   Interim European Centre for Medium-Range Weather Forecasts (ECMWF)

96   Re-Analysis (ERA-Interim) products. We used GPS datasets from Hong Kong in

97   August 2016 to evaluate this new method. The results demonstrate better accuracy

98   than those of the traditional method with radiosonde data.

99   The rest of this paper is organized as follows. Section 2 introduces the principles of

100   GNSS tomography and the optimized technique for establishing the atmospheric

101   weighted average temperature model and deriving the scale height of water vapor.

102   Section 3 describes the data processing. Section 4 presents the validation of the

103   optimized method, and the quality control process for the tomography results. The

104   discussions and conclusions are given in Section 5.

105   **2.   GNSS Tomographic formulation**

106   In this section, we first introduce the GPS tomography model. We then illustrate the

107   optimized techniques for the ZHD model and the humidity conversion coefficient

108   determination. Finally, we present the constraint model.

109   2.1 Tomographic technique

110   To reconstruct 3D images of water vapor density distributions, the SWV along ray

111   paths traversing the imaged region should first be obtained from dual-frequency

112   GNSS data. This is defined by the line integral of water vapor density along the ray

113   path from satellite to receiver (Flores et al., 2001), as follows:

114 $$SWV = \frac{1}{\rho_w} \cdot \left(\int_s \rho(s) ds \right) \tag{1}$$

115 where ρ_w means the density of liquid water, s denotes the trajectory of GNSS signals

116 in the troposphere, and $\rho(s)$ indicates the water vapor density.

117 Eq. (1) reveals that the accuracy of water vapor density mainly depends on the

118 quality of the SWV. Generally, ZTD can be precisely estimated using the

119 double-difference or PPP method. ZWD can be obtained by removing ZHD from

120 ZTD. After the humidity conversion coefficient is determined, the SWV will be

121 computed providing that the SWD is known (MacMillan, 1995), as follows:

122 $$SWD = STD - SHD - \Delta L_{gradient} \tag{2}$$

123 $$\Delta L_{gradient} = \frac{1}{sin(e) \cdot tan(e) + C} \cdot \left(G_N \cdot cos(\alpha) + G_E \cdot sin(\alpha) \right) \tag{3}$$

124 $$PWV = \Pi \cdot ZWD \tag{4}$$

125 $$SWV = \Pi \cdot SWD \tag{5}$$

126 where STD and SHD are slant troposphere delay and slant hydrostatic delay,

127 respectively; $\Delta L_{gradient}$ means the horizontal gradient; G_N and G_E are the north and east

128 atmosphere horizontal gradients, respectively; e and α are the satellite elevation angle

129 and the azimuth angle, respectively; C is a constant with as $C=0.003$ (Chen and

130 Herring, 1997); and Π means the humidity conversion coefficient. SWD and SHD can

131 be projected to ZWD and ZHD based on the Niell mapping function (Niell, 1996).

132 From Eq. (2) and Eq. (5), we know that the accuracy of the ZHD and the humidity

133 conversion coefficient are the crucial aspects that affect SWV quality. Thus, it is

134 essential to develop a high-precision ZHD model and humidity conversion coefficient.

135 2.2 Humidity conversion coefficient

136   The humidity conversion coefficient Π can be expressed as a function of T_m. T_m varies

137   across seasons and areas and depends mainly on the surface atmosphere temperature

138   (Bevis et al., 1994), as follows:

139
$$\Pi = \frac{10^6}{\rho_w \cdot \frac{R}{m_w} \cdot \left[\frac{k_3}{T_m} + k_2 - \frac{m_w}{m_d} \cdot k_1 \right]} \qquad (8)$$

140
$$T_m = \frac{\int_{h_0}^{\infty} \left(P_w / T \right) \cdot dh}{\int_{h_0}^{\infty} \left(P_w / T^2 \right) \cdot dh} = \frac{\sum \frac{(h_2 - h_1) P_w}{T}}{\sum \frac{(h_2 - h_1) P_w}{T^2}} \qquad (9)$$

141   where ρ_w is the density of liquid water; k_1, k_2 and k_3 are constants—$k_1 = 77.6$ K/hPa, k_2

142    $= 70.4$ K/hPa and $k_3 = 3.739*10^5$ K/hPa (Bevis, 1994); T_m is the atmospheric weighted

143   average temperature; m_d and m_w mean the molar masses of dry atmosphere and water

144   vapor, respectively; R indicates the universal gas constant; P_w indicates water vapor

145   pressure in units of hPa; T is the atmosphere temperature and h means the height.

146   2.3 Constraint model

147   Usually, the observation equation of the tomographic approach is rank deficient

148   because the GPS signal cannot pass through all of the grids. Horizontal constraints,

149   vertical constraints, priori information value constraints, and boundary constraints

150   must be added to avoid this deficiency. With these constraints, we can use an iterative

151   reconstruction algorithm, or a non-iterative reconstruction algorithm to resolve the

152   tomography equation.

153   The horizontal constraint is the Gauss distance weighting function (Song, 2004), as

154   follows:

155
$$B = \frac{\exp^{\frac{-d_{i,j,k}^2}{2\delta^2}}}{\sum_{i=1}^{nl}\sum_{j=1}^{nn}\exp^{\frac{-d_{i,j,k}^2}{2\delta^2}}}$$
(10)

156   where B is the horizontal smoothing; the subscript i,j,k means the index of voxel in 3D

157   space; nl and nn are the numbers of the grids in the east–west and north–south

158   directions, respectively; $d_{i,j,k}$ indicates the distance between known and unknown

159   water vapor grids; and δ denotes the smoothing factor, which will change at different

160   levels. Section 3.3.1 explains how to estimate δ.

161   The vertical distribution of water vapor does not follow the ideal-gas law,

162   particularly in the lower levels. Currently, there is no accurate model function to fit the

163   spatial distribution of water vapor. The vertical constraint of atmospheric tomography

164   can be obtained using an exponential model (Jiang et al., 2014; Ye et al., 2016), as

165   follows:

166    $\rho(h) = \rho_0 \cdot exp\left(-\frac{h-h_0}{H_{we}}\right)$ (11)

167   where $\rho(h)$ is the water vapor density at the height of h; ρ_0 is the water vapor density at

168   the height of h_0; and H_{we} is the scale height of water vapor. ρ_0, h_0 and H_{we} can usually

169   be determined using radiosonde or COSMIC historical data. In this case, the estimated

170    $\rho(h)$ is only an experience value and will have a greater error than the true value.

171   Therefore, we propose a new method to estimate $\rho(h)$ and H_{we} in near-real-time.

172   Based on Eq. (2) and the Niell mapping function (Niell, 1996), ZWD can be

173   estimated in real-time. PWV can then be obtained according to Eq. (4). The

174   relationship between PWV and $\rho(h)$ is established as follows:

175    $PWV = \frac{1}{\rho_w} \cdot \int_{h_0}^{h_{top}} \rho(h)dh$ (12)

176   where ρ_w is the density of liquid water; h_0 is the height of station and h_{top} is the

177   height of tropopause. Combining Eq. (11) and Eq. (12), we get:

178     $PWV =$

179     $\frac{1}{\rho_w} \cdot \int_{h_0}^{h_{top}} \rho(h) dh = \frac{1}{\rho_w} \cdot \int_{h_0}^{h_{top}} \rho_0 \cdot exp\left(-\frac{h-h_0}{H_{we}}\right) dh = \frac{\rho_0 \cdot H_{we}}{\rho_w}\left[1 - exp\left(-\frac{h_{top}-h_0}{H_{we}}\right)\right] \cong$

180     $\frac{\rho_0 \cdot H_{we}}{\rho_w}$ (13)

181   The parameter H_{we} can be derived in real-time using Eq. (13). Based on Eqs. (11)

182   and (13), Eq. (14) can be utilized to establish the functional relationship in the vertical

183   direction, as follows:

184     $\frac{\rho_{i,j,k+1}}{\rho_{i,j,k}} = exp^{-\left(\frac{h_{k+1}-h_k}{h_{we}}\right)}$ (14)

185   where $\rho_{i,j,k}$ represents the water vapor value of datum voxel (i,j,k).

186   The priori humidity information can be used for the background field of troposphere

187   tomography, and will enhance the computing speed and tomography accuracy. The

188   synoptic observation data include the atmosphere pressure, atmosphere temperature,

189   and relative humidity observed in the station and the atmosphere temperature and

190   relative humidity can be interpolated into all of the voxels using Eqs. (10) and (14).

191   Thus, the water vapor density of every voxel can be calculated (Jiang et al., 2014).

192   **3. Data processing**

193   3.1 Data collection

194   Data used to remote sense atmospheric water vapor contain ground-based GNSS

195   observations and meteorological data, and space-based COSMIC wet profiles.

196   UCAR/CDAAC supplies two different types of products: real-time profiles and

197   post-processed profiles. The former can be available within a few hours and the latter

198   can be available with a 6-week latency (www.cosmic.ucar.edu). We selected

199   post-processed profiles in this study. Wet profiles (wetPrfs) are one type of COSMIC

200   post-processed products that are freely available for public access

201   (http://cdaac-www.cosmic.ucar.edu/cdaac/). wetPrfs are interpolated products

202   sampled at 100-m intervals and obtained using a nonstandard one-dimensional

203   variation technique together with European Centre for Medium-Range Weather

204   Forecasts (ECMWF) low-resolution analysis data from altitude of the perigee point

205   from the surface to a 40-km altitude (CDAAC., 2005a). The average bias of

206   temperature between wetPrfs and radiosonde is less than 0.1 K, 70% - 90% of the

207   wetPrfs reach to within 1 km of the surface on a global basis.

208   (http://www.cosmic.ucar.edu/ro.html).

209   We used ground-based GNSS observations and meteorological products from the

210   Hong Kong SatRef network (https://www.geodetic.gov.hk/), from 12 continuously

211   operating reference stations with an inter-station distance of 7 to 27 km, covering

212   approximately 1100 km^2. All 12 stations were equipped with "LEICA

213   GRX1200+GNSS" receivers and had data sampling rates of 5 seconds, as shown in

214   Fig. 1. The meteorological data associated with each GPS station at 60-second

215   intervals is freely available at https://www.geodetic.gov.hk/. GPS datasets from

216   August 1, 2016 to August 31, 2016 were collected daily in Hong Kong. wetPrfs in or

217   near Hong Kong in August of 2009–2015 were downloaded.

218
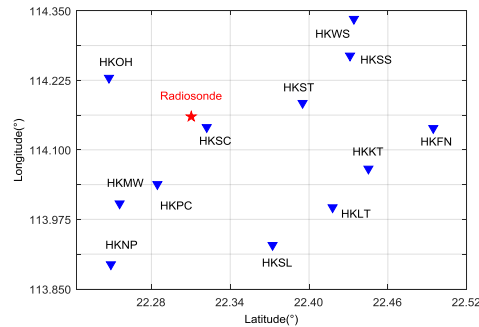
Fig. 1. Distribution of the Hong Kong SatRef sites (blue triangles) inside the tomography

219

horizontal grid (black dotted lines) and the KingPark radiosonde station (red star). The region was

220

discretized into an $8 \times 5 \times 17$ cell grid for the GPS water vapor tomography. The layer heights are

221

0, 400, 800, 1400, 2000, 2600, …, 8600 from ground to water vapor layer top.

222

223

The reconstruction region covered an area ranging from latitude 22.22 to 22.52 °N,

224

longitude 113.85 to 114.35 °E, and from ground to water vapor layer top (WVLT) in

225

height. Thus, the entire area of Hong Kong was divided in to 5×8 horizontal grids

226

and 17 vertical layers. A total of $8 \times 5 \times 17 = 680$ voxels were divided in the 3-D

227

space.

228

3.2 Regional weighted average temperature model

229

Bevis et al. (1994) first put forward the global T_m model using radiosonde products.

230

Later, Wang et al. (2011) established the T_m model in Hong Kong using radiosonde

231

products. Ye et al. (2016) also assessed the relationship between T_m and surface

232

temperature based on radiosonde and COSMIC products. However, these three

233

models only consider the parameter of surface temperature. We propose considering

234

235 the effects of temperature and height to establish a T_m model using COSMIC products.

236 The new model is given as follows (Yao et al., 2013):

237 $$TmN = a + b \cdot T_h + c \cdot T_h^2 + e \cdot h + f \cdot h^2 \qquad (15)$$

238 where a, b, c, e and f are constants that can be determined using COSMIC products;

239 T_h indicates the temperature at height h; h denotes the height; and TmN is the new

240 model value of T_m.

241   The weighted average temperature T_m is obtained using Eq. (9) with input wet

242 pressure and temperature provided from wetPrfs. TmN can be derived using Eq. (15);

243 its values are shown in Fig. 2. The wetPrfs described in Section 3.2 are used to derive

244 the humidity conversion coefficient from Eq. (8).
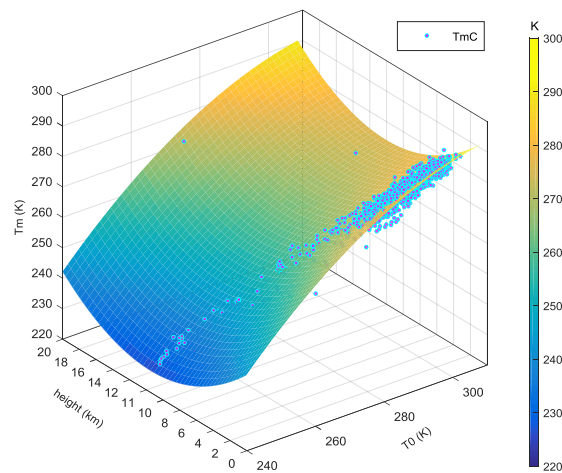
245

246 **Fig. 2.** Considering height and surface temperature to establish the T_m model using wetPrf

247   products. T_0 is the surface temperature; and TmC is the fitted atmospheric weighted average

248   temperature obtained from COSMIC products for 2009 to 2015 in Hong Kong.

249

250   As shown in Fig. 2, the new model's T_m values agree well with the true values. To

251   evaluate the new T_m model, its values are compared with those obtained from

252   radiosonde and COSMIC products. Fig. 3 shows the results for Hong Kong in August

253   2016.
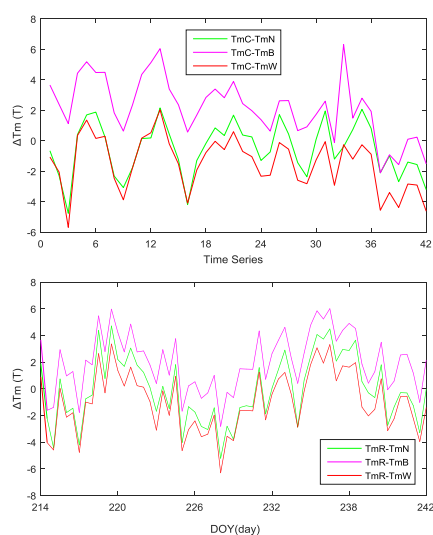
254

255   **Fig. 3.** New T_m model values are compared with those derived from COSMIC and

256   radiosonde products in Hong Kong in August 2016. TmC is the T_m derived from COSMIC

257   products; TmN is the T_m derived from the new model; TmB is the T_m derived from the Bevis model;

258   TmW is the T_m derived from the Wang model; and TmR is the T_m derived from radiosonde

259   products.

260

261   The statistical results comparing the model-derived and COSMIC-derived T_m are

262   given in Table 1. We provide a summary of the T_m deviation between

263   radiosonde-derived and model-derived data in Table 2.

264   **Table 1.** Summary of the T_m deviation between COSMIC-derived and model-derived (K) data.

	Max.	Min.	Mean	RMS
TmC-TmN	2.2	-4.7	-0.5	1.7
TmC-TmB	6.3	-2.1	2.2	2.9
TmC-TmW	2.1	-5.7	-1.5	2.3

265   **Table 2.** Summary of the T_m deviation between radiosonde-derived and model-derived (K) data.

	Max.	Min.	Mean	RMS
TmR-TmN	4.7	-5.2	-0.1	2.4
TmR-TmB	6.1	-2.8	2.1	3.0
TmR-TmW	3.4	-6.4	-0.9	2.4

266   As shown in Tables 1 and 2, the new T_m model improves the accuracy of

267   atmospheric weighted average temperature from the Bevis model and Wang

268   model.

269   3.3 Tomography constraint condition

270   3.3.1 Estimating the smoothing factor

271   The smoothing factor δ in Eq. (10) is an uncertain parameter in the horizontal

272   constraint. Usually, it is assigned a constant value of experience (Xia et al., 2013;

273   Jiang et al., 2014). Because δ varies with regions and seasons and also changes with

274   different levels of tomography model, ERA-Interim data for Hong Kong from August

275   2009 to August 2015 were used to precisely estimate δ. ERA-Interim is a reanalysis of

276   the global atmosphere covering the data-period since 1989, and continuing in real

277   time (http://apps.ecmwf.int/datasets/data/). The specific humidity data with 60 levels

278   of vertical spatial resolution and a minimum grid of 0.125 °*0.125 ° are publicly

279   available. The main characteristics of the ERA-Interim system and many aspects of its

280   performance are described in ECMWF newsletters 110, 115, and 119

281   (http://www.ecmwf.int/publications/newsletters).   In   addition,   comprehensive

282   documentation of ERA-Interim, including observation usage, is currently being

283   prepared and will be made available at http://www.ecmwf.int/research/era.

284   In each level, the humidity information of one grid point equals the weighted

285   average of its neighbors (Rius et al., 1997), as follows:

286    $$0 = B_1\rho_1 + B_2\rho_2 + \cdots + B_{j-1}\rho_{j-1} - \rho_j + B_{j+1}\rho_{j+1} + \cdots \qquad (16)$$

287   According to the humidity information provided by ERA-Interim, Eq. (16) can be

288   solved using the optimal parameter search method. The search step is set to 1 and the

289   search range is [0, 20]. The value of δ is exactly equal to the number of grid points in

290   each level, and we defined the mean of δ as the smoothing factor of the level. Table 3

291   lists the δ values at different heights using ERA-Interim data for Hong Kong from

292   August 2009 to August 2015.

293   **Table 3.** Smoothing factor derived by ERA-Interim products at different heights.

Height range (km)	0	0.4	0.8	1.4	2	2.6	3.2	3.8	4.4	5.0	5.6	6.2	6.8	7.4	8.0	8.6
δ (integer)	8	8	7	6	5	8	4	7	6	6	4	4	4	4	4	4

294   Table 3 shows that the smoothing factors present a nonlinear change for increasing

295   heights below 6 km, but do not change between 6 and 9 km. The horizontal constraint

296   can be accurately determined based on the smoothing factor and the distance between

297   known and unknown grids.

298   3.3.2 Vertical constraint

299   The purpose of GNSS tomography technique is to derive the 3-D distribution of water

300   vapor. Thus, the accuracy of the vertical constraint will directly affect the quality of

301   the tomography results. Because water vapor randomly varies in time-space, it is

302   difficult to precisely probe the spatial distribution of water vapor. Traditionally, Eq.

303 (14) was used as a vertical constraint and the parameter H_{we} could be obtained using

304 COSMIC or radiosonde historical data products (Ye et al., 2013; 2016). Due to H_{we}

305 changes over time are obvious, so they need to be obtained once for each tomography

306 epoch. In this paper, PWV was derived using Eq. (4), and H_{we} was then derived in real

307 time based on Eq. (13). To evaluate the accuracy of H_{we}, the radiosonde-obtained

308 water vapor is used as references to assess the water vapor calculated using Eq. (11).

309 The statistical results are given in Table 4 using the "45004th" radiosonde station (lat:

310 22.32; lon: 114.16) and HKSC station (lat: 22.32; lon: 114.14) datasets from August

311 2016 under 10 km.

312 **Table 4.** Statistical results from Eq. (11)-derived and radiosonde-derived PWV (g/m^3). RWV is the

313   water vapor density obtained from the radiosonde product; TWV is the water vapor density

314 derived from the H_{we} obtained by the traditional method using Eq. (11); NWV is the water vapor

315   density derived from the H_{we} obtained by the new method using Eq. (11).

	RMS	Mean
RWV-TWV	8.29	-3.29
RWV-NWV	5.15	-2.87

316   As shown in Table 4, the water vapor density derived from the H_{we} obtained using

317 the new technique and Eq. (11) is closer to the radiosonde-derived water vapor density.

318 Therefore, it is more reasonable to use the H_{we} obtained using the new technique and

319 Eq. (14) as the vertical constraint.

320 **4. Result validation and analysis**

321 To evaluate our optimized method, we obtained ZTDs from the Hong Kong SatRef

322 network in August 2016, based on Bernese 5.2 (non-difference) software. The ZHDs

323   were estimated using the Saastamoinen mode. The SWV was then obtained using the

324   Niell mapping function (Niell, 1996) and the calibrated humidity conversion

325   coefficient. The WVLT was determined as 9.5 km from COSMIC historical data and

326   Ye et al.'s (2016) method. Following the tomography model proposed by Flores et al.

327   (2000), we estimated the 3D water vapor distribution using the GPS tomography

328   technique with the horizontal constraint from Eq. (10) and the vertical constraint from

329   Eq. (14). The tomography equation was solved adopting Kalman filtering. The

330   tomography results were outputted once every 30 minutes. As we have limited space,

331   Fig. 4 only shows the 3D distribution of water vapor density on August 1, 2016 and

332   August 2, 2016.
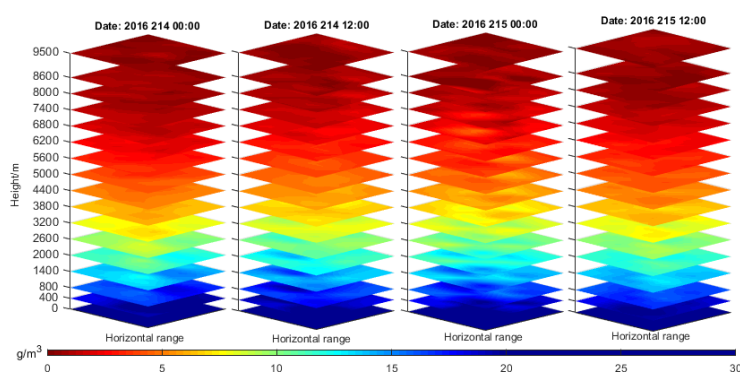
333

334   **Fig. 4.** 3D tomographic water vapor distribution in Hong Kong on August 1, 2016 and August 2,

335   2016.

336

337   Figure 4 presents the 3D tomographic water vapor distribution in Hong Kong for

338   heights lower than 9.5 km. The results show that the water vapor changes significantly

339   below 3.8 km, whereas it remains stable above 3.8 km. In addition, the water vapor is

340   mainly concentrated blow 2.6 km.

341   4.1 Compare the results between tomography-obtained and radiosonde-obtained

342   Radiosonde products contain 3-D distribution of meteorological elements such as

343   atmosphere temperature, atmosphere pressure, mixing ratio, and relative humidity. The

344   "wet" pressure can be obtained based on the pressure and mixing ratio and can be

345   utilized to compute the water vapor density (Song, 2004). To verify the advantage of

346   the optimized GPS tomography method, using radiosonde products as references, the

347   tomography results were compared with those derived from the traditional tomography

348   technique using the Saastamoinen dry model, traditional humidity conversion

349   coefficient (0.1538), smoothing factor (10) and H_{we} obtained using the traditional

350   technique and COSMIC historical products. Fig. 5 compares the water vapor densities

351   derived from radiosonde products and the traditional and optimized tomography

352   techniques for August 1, 2016 and August 2, 2016.
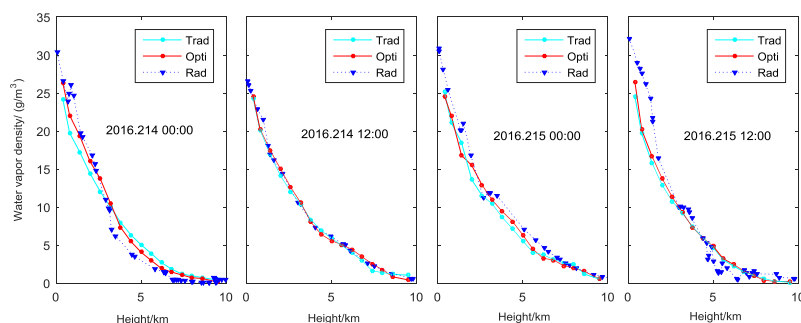
353

354   **Fig. 5.** Water vapor densities obtained from tomography-derived and radiosonde-derived data. Rad

355   is the water vapor density derived using radiosonde products; Trad is the water vapor density

356   derived using the traditional tomography method; and Opti is the water vapor density derived

357   using the optimized method.

358   It can be observed in Fig. 5 that the changing trends of water vapor with height

359   across the tomography-obtained and radiosonde-obtained have a good agreement.

360   However, when the "inversion layer" occurs, GPS tomography cannot accurately

361   reflect this situation. In Table 5, we present the deviation statistics for GNSS

362   tomography-obtained and radiosonde-obtained water vapor density at heights above

363   and below 3.8 km, using 31-day datasets from Hong Kong over the whole of August

364   2016.

365   **Table 5.** Statistics for tomography-derived and radiosonde-derived water vapor density above and

366   below 3.8 km (g/m^3). Rad is the radiosonde-derived water vapor density; Opti is the optimized

367   tomography-derived water vapor density; and Trad is the traditional tomography-derived water

368   vapor density.

Height		Lower 3.8 km		Upper 3.8 km	
		Bias	RD	Bias	RD
Mean	Rad-Opti	-1.45	-18.76%	0.56	29.87%
	Rad-Trad	-1.88	-24.32%	0.74	39.45%
RMS	Rad-Opti	2.61	33.76%	0.91	48.38%
	Rad-Trad	3.03	38.94%	0.99	52.37%

369   Table 5 provides the statistics values of the differences between GNSS

370   tomography-obtained and radiosonde-obtained results. As seen from the statistical

371   results, the RMS and mean values of troposphere tomography using the optimized

372   technique is less than than that based on the traditional method for altitudes below 3.8

373   km. In addition, compared with the radiosonde data, the test results show that the

374   water vapor density quality obtained by the optimized technique is 13.8% better

375   below 3.8 km and 8.1% better above 3.8 km than that obtained by the traditional

376   technique.

377   4.2 Quality of GPS tomography technology

378   We also studied the differences in the entire humidity profile between the

379   tomography-derived and radiosonde-derived results. We used the root mean square

380   (RMS) and Pearson product-moment correlation coefficient (PCC) as the evaluation

381   index correlated between the two profiles. PCC is a commonly used measure of the

382   degree of correlation of two sequences of parameters, and the mathematical model is

383   as follows (Lee Rodgers and Nicewander, 1988):

384
$$PCC = \frac{\sum_{i=1}^{N}(X_i - \overline{X_i})(Y_i - \overline{Y_i})}{\sqrt{\sum_{i=1}^{N}(X_i - \overline{X_i})^2} \cdot \sqrt{\sum_{i=1}^{N}(Y_i - \overline{Y_i})^2}} \qquad (17)$$

385   Fig. 6 presents the PCC and RMS of tomography results (traditional and optimized)

386   for August 2016. Here we set up a set of criteria to evaluate the tomography profile

387   PCC > 0.90 and RMS < 2.0 g/m^3. When GPS tomography results meet these criteria,

388   they are considered a success. According to the criteria, the success rate of the

389   inversion is shown in Table 6.
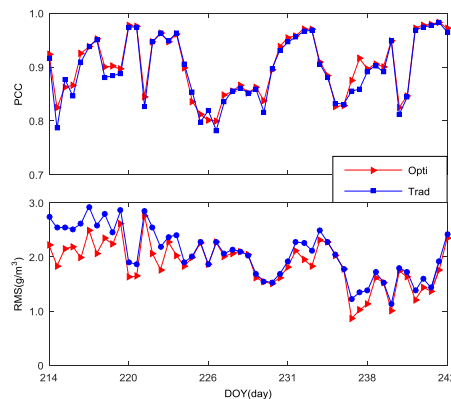
390

391 **Fig. 6.** Time series of PCC and RMS for August 2016. Opti is the optimized tomography-derived

392   water vapor density; and Trad is the traditional tomography-derived water vapor density.

393   **Table 6.** Statistical results of PCC and RMS for August 2016 (%).

	Trad	Opti
PCC	66.29	55.57
RMS	60.14	51.43
PCC and RMS	48.07	38.36

394   As shown in Table 6, the success rate of the optimized technique is nearly 10%

395 higher than that of the traditional technique, and the degree of improvement is evident.

396 In fact, the principles of radiosonde and GPS tomography techniques are different.

397 Radiosonde products reflect the state of the atmosphere at a certain time at the

398 instrument's location, but GPS tomography techniques mirror the average water vapor

399 state. Thus, it is difficult to determine an absolute standard to evaluate the success of

400 GPS tomography results.

401 **5. Conclusions**

402 In this study, several key techniques in the GNSS tomography method were optimized

403 to improve the accuracy of water vapor density. First, we re-established an

404 atmospheric weighted average temperature model using COSMIC wetPrfs. According

405 to the spatial distributions of water vapor provided by COSMIC products, we used the

406 exponential model to fit the vertical variation of water vapor. The exponential function

407 is usually utilized as the vertical constraint, and we proposed a new method to

408 compute the scale height of water vapor. We determined the smoothing factor of the

409 Gauss distance weighting function using ERA-Interim products. Finally, we used GPS

410   datasets from Hong Kong in August 2016 to compute the PWV and the vertical

411   distribution of water vapor density.

412   To evaluate the quality of the optimized technique, we compared the optimized and

413   traditional technique results with radiosonde-obtained water vapor. The statistical

414   results show that the water vapor density quality obtained by the optimized technique

415   is 13.8% better below 3.8 km and 8.1% better above 3.8 km than that obtained by the

416   traditional technique. We then calculated the success rate of tomographic inversion

417   according to PCC and RMS. The statistics show that the success rate of the optimized

418   technique was approximately 10% higher than that of the traditional technique.

419   **References**

420   Beyerle, G., Schmidt, T., Michalak, G., 2005. GPS Radio Occultation with GRACE:

421   Atmospheric profiling utilizing the zero difference technique. Geophys. Res. Lett.

422   32, L1386.

423   Bevis, M., Businger, S., Herring, T., Rocken, C., Anthes, R., Ware, R., 1992. GPS

424   meteorology: Remote sensing of atmospheric water vapor using the global

425   positioning system, J. Geophys. Res. 94, 15787-15801.

426   Bevis, M., Businger, S., Chiswell, S., Herring, T.A., Anthes, R.A., Rochen, C., Ware,

427   R.H., 1994. GPS Meteorology: Mapping zenith wet delays onto precipitable water.

428   J. Appl. Meteorol. 33, 379-386.

429   CDAAC., 2005a. Algorithms for inverting Radio Occultation signals in the neutral

430   atmosphere, COSMIC Project Office. University Corporation for Atmospheric

431   Research. http:// cosmic-io.cosmic.ucar.edu/cdaac/doc index.html

432   Champollion, C., Masson, F., Bouinm, N., 2005. GPS water vapor tomography:

433   Preliminary results from the ESCOMPTE field experiment. Atmos. Res. 74(1-4),

434   253-274.

435   Chen., B., Liu., Z., 2014. Voxel-optimized regional water vapor tomography and

436   comparison with radiosonde and numerical weather model. J. Geod. 88, 691-703.

437   Davis, J.L., Herring, T.A., Shapiro, I.I., Rogers, A., Elgered, G., 1985. Geodesy by

438   radio interferometry: Effects of atmospheric modeling errors on estimates of

439   baseline length. Radio Sci. 20, 1593-1607.

440   Esteban, E., Vazquez, B., Borota, A., Grejner, B., 2013. GPS-PWV estimation and

441   validation with radiosonde data and numerical weather prediction model in

442   Antarctica. GPS Solut. 17, 29-39.

443   Falconer, R.H., Cobby, D., Smyth, P., Astle, G., Dent, J., Golding, B., 2009. Pluvial

444   flooding: New approaches in flood warning, mapping and risk management. J.

445   Flood Risk Manag. 2, 198-208.

446   Flores, A., Ruffini, G., Rius, A., 2000. 4D tropospheric tomography using GPS slant

447   wet delays. Ann. Geophys. 18, 223-224.

448   Hajj, G.A., Kursinski, E.R., Romans, L.J., Bertiger, W.I., Leroy, S.S., 2002. A

449   technical description of atmospheric sounding by GPS occultation. J. Atmos. Sol.

450   Terr. Phys. 64(4), 451-469.

451   Jacob, D., Brring, L., Christensen, O., Christensen, J., De Castro, M., Dqu, M.,

452   Giorgi, F., Hagemann, S., Hirschi, M., Jones, R., Kjellstrm, E., Lenderink, G.,

453   Rockel, B., Snchez, E., Schr, C., Seneviratne, S., Somot, S., van Ulden, A., van den

454   Hurk, B., 2007. An inter-comparison of regional climate models for Europe: Model

455   performance in present-day climate. Clim. Change. 81(12), 8479-8491.

456   Jin, S.G., Park, J.U., 2007. GPS ionospheric tomography: A comparison with the

457   IRI-2001 model over South Korea. Earth Planets Space. 59(4), 287-292. doi:

458   10.1186/BF03353106

459   Jin, S.G., Park, J., Cho, J., Park, P., 2007. Seasonal variability of GPS-derived Zenith

460   Tropospheric Delay (1994-2006) and climate implications. J. Geophys. Res. 112.

461   D09110, doi: 10.1029/2006JD007772

462   Jin, S.G., Li., Z.C., Cho, J.H., 2008. Integrated water vapor field and multi-scale

463   variations over China from GPS measurements. J. Appl. Meteorol. Clim. 47(11),

464   3008-3015. doi: 10.1175/2008JAMC1920.1

465   Jin, S.G., Luo, O.F., Gleason, S., 2009. Characterization of diurnal cycles in ZTD

466   from a decade of global GPS observations. J. Geodesy. 83(6), 537-545. doi:

467   10.1007/s00190-008 -0264-3

468   Jin, S., Luo, O., 2009. Variability and climatology of PWV from global 13-year GPS

469   observations. *IEEE* Trans. Geosci. Remote Sens. 47(7), 1918-1924. doi:

470   10.1109/TGRS.2008.2010401

471   Jin, S.G., Feng, G.P., Gleason, S., 2011. Remote sensing using GNSS signals: Current

472   status and future directions. Adv. Space Res. 47(10), 1645-1653. doi:

473   10.1016/j.asr.2011.01.036

474   Jiang, P., Ye, S.R., Liu, Y.Y., Zhang, J.J., Xia, P.F., 2014. Near real-time water vapor

475   tomography using ground-based GPS and meteorological data: Long-term

476   experiment in Hong Kong. Ann. Geophys. 32, 911-923.

477   Kishore, P., Venkat, R., Namboothiric, S.P., Velicognaa, I., Bashab, G., Jiang, J.H.,

478   Igarashi, K., Rao, S.V.B., Sivakumar,V., 2011. Global

479   (50 °S-50 °N) distribution of water vapour observed   by   Cosmic

480   GPS Ro: Comparison with GPS Radiosonde,   NCEP, Era-Interim, and   Jra-25

481   reanalysis data sets. J. Atmos. Sol. Terr. Phy. 73, 1849-1860.

482   Kouba, J., Heroux, P., 2001. Precise point positioning using IGS orbit and clock

483   products, GPS Solut., 5(2), 12-28.

484   Kuo, B., Rocken, C., Anthes, R., 2007. GPS Radio Occultation Missions. The second

485   Formosat3/COSMIC Data Users Workshop, Boulder, Colorado.

486   Kursinski, E.R., Hajj, G.A., Schofield, J.T., 1997. Observing Earth's atmosphere with

487   Radio Occultation measurements using the Global Positioning System.

488   J.Geophs.Res. 102(D19), 23428-23465.

489   Lee, R.J., and Nicewander, W.A., 1988. Thirteen ways to look at the correlation

490   coefficient, Am. Stat., 42, 59-66, 1988.

491   Liu, Y., Iz, H.B., Chen, Y., 2000. Precise determination of dry zenith delay for GPS

492   meteorology applications. Acta Geod. Cartogr. Sin. 29(2), 172-179

493   Liu, Y., Chen, Y., 2002. Improving accuracy of near real-time precipitable water

494   vapor estimation with the IGS predicted orbits. Geophys. Res. Lett. 29(16),

495   411-413.

496   Notarpietro, R., Cucca, M., Gabella, M., 2011. Tomographic reconstruction of wet and

497   total refractivity fields from GNSS receiver networks. Adv. Space Res. 898-912.

498   Doi:10.1016/j.asr.2010.12.025

499   Notarpietro, R., Gabella, M., Perona, G., 2008. Tomographic reconstruction of neutral

500   atmospheres using slant and horizontal wet delays achievable through the

501   processing of signal observed from small GPS networks. Ital. J. Remote Sens. 40(2),

502   63-74.

503   Nilsson, T., Gradinarsky, L., 2006. Water vapor tomography using GPS phase

504   observation: Simulation results. IEEE Trans. Geosci. Remote Sens. 44, 2927-2941.

505   Niell, A.E., 1996. Global mapping functions for atmosphere delay at radio

506   wavelengths. J. Geophys. Res. 101, 3227-3246.

507   Mateus, P., Nico, G., Catalao, J., 2014. Maps of PWV temporal changes by SAR

508   interferometry: A study on the properties of atmosphere's temperature profiles.

509   IEEE Geosci. Remote S. 11(12), 2065-2069.

510   Perler, D., Geiger, A., Hurter, F., 2011. 4D GPS water vapour tomography: New

511   parameterized   approaches.   J.   Geophys.   85,   539-550.

512   doi:10.1007/s00190-011-0454-2

513   Rius, A., Ruffini, G., Cucurull, L., 1997. Improving the vertical resolution of

514   ionospheric tomography with GPS occultations. Geophys. Res. Lett. 24,

515   2291-2295.

516   Rocken, C., Anthes, R., Exner, M., Hunt, D., Sokolovskiy, S., Ware, R., 1997.

517   Analysis and validation of GPS/MET data in the neutral atmosphere. J. Geophys.

518   Res. 102(D25), 29849-29866.

519   Skone, S., Hoyle, V., 2005. Troposphere modeling in a regional GPS network. Journal

520   of global positioning systems. 4(1-2), 230-239. Doi: 10.5081/jgps.4.1.230

521   Shi, J., Gao, Y., 2009. Assimilation of GPS radio occultation observations with a near

522   real-time GPS PPP-inferred water vapour system. Proceedings of ION GNSS,

523   Savannah, Georgia. 2584-2590.

524   Song, S.L., 2004. Sensing three dimensional water vapor structure with ground-based

525   GPS network and the application in meteorology. Ph.D. thesis of Shanghai

526   Astronomical Observatory CAS. 80-84.

527   Troller, M., Geiger, A., Brockmann, E., Kahle, H-G., 2006. Determination of the

528   spatial and temporal variation of tropospheric water vapor using CGPS networks.

529   Geophys. J. Int. 167(2), 509-520.

530   Wang, X., Song, L., Dai, Z., Cao, Y., 2011. Feature analysis of weighted mean

531   temperature Tm in Hong Kong. J. Nanjing Univ. Info. Sci. Tech. 3, 47-52.

532   Wang, B.R., Liu, X., Wang, J., 2013. Assessment of COSMIC radio occultation

533   retrieval product using global radiosonde data. Atmos. Meas. Tech. 6, 1073-1083.

534   Xia, P., Cai, C., and Liu, Z., 2013. GNSS troposphere tomography based on two-step

535   reconstructions using GPS observations and COSMIC profiles. Ann. Geophys. 31,

536   1-11.

537   Yao, Y.B., Zhang, B., Yue, S.Q., Xu, C.Q., Peng, W.F., 2013. Global empirical model

538   for mapping zenith wet delays onto precipitable water. J. Geod. 87: 439-448. doi

539   10.1007/s00190-013-0617-4

540   Yen, N.L., Huang, Chen, J.F., 2007. FORMOSAT-3/COSMIC GPS radio occultation

541   mission: Preliminary results. TEEE T. Geosci. Remote. 45, 3813-3825.

542   Ye, S., Jiang, P., Liu, Y., 2013. A water vapor tomographic numerical quadrature

543   approach with ground-based GPS network. Acta Geod. Cartogr. Sin. 42(5),

544   654-660.

545   Ye, S., Xia, P., and Cai, C., 2016. Optimization of GPS water vapor tomography

546   technique with radiosonde and COSMIC historical data. Ann. Geophys. 34, 1-11.